中國機械工程學刊第四十四卷第二期第 121~131 頁(民國一百一十二年)
Journal of the Chinese Society of Mechanical Engineers, Vol.44, No.2, pp121~131 (2023)

Enhancement of Thermal Strength and Corrosive Resistance for Rotating Cylindrical Tubes Made of FGC and FGM Using CVD-SiC and T91 When Subjected to High-temperature Sources of Gaussian Laser Boundaries

Hsin-Yi Lai * and Kai-Chien Lo*

Keywords: functionally graded material, maximum shear stress, corrosion resistance

ABSTRACT

Materials such as CVD-SiC and T91 martensitic-ferritic are widely used as nuclear fuel cladding base material for LWRs (light water reactors) due to their excellent high temperature and corrosive resistance under critical environmental conditions. This study is geared towards investigation of the functional graded composites (FGC) of CVD-SiC-$Fe_{12}Cr_2Si$ and the functional graded material (FGM) of T91-$Fe_{12}Cr_2Si$, respectively, to meet the needs of thermal impact of LWR industry. The work-piece in a wide range of high temperature environment from 20°C to 1200°C is implemented and simulated using a 3D rotating cylindrical tube and a 2D cylindrical model with a laser quenching boundary.

The linear rule of mixture and Wakashima-Tsukamoto estimate are the main algorithms of FGM in this study. The continuous material property distribution of FGM material can prevent stress concentration and non-continuous problem of diffusion in the rotating cylindrical tube and the associated 2D cylindrical model. Moreover, the silicon concentration of the 2D cylindrical model on the inner surface can be transformed to an oxidized layer, which enhances the corrosive resistance of FGC and FGM models.

The margin of safety calculated by the tresca stress is also promoted when the volume mixture number of FGM material is increased, and the materials are designed based on the $Fe_{12}Cr_2Si$- SiC model. This result shows the $Fe_{12}Cr_2Si$-SiC FGM model with a volume mixture number of three is an ideal material component for nowadays fuel cladding design being aware of LBLOCA problem.

Paper Received March, 2023. Revised March, 2023, Accepted March, 2023, Author for Correspondence: Kai-Chien Lo.

**Ph.D. Candidate, Department of Mechanical Engineering, National Cheng Kung University, Tainan, Taiwan, ROC.*

*** Distinguished Professor, Department of Mechanical Engineering, National Cheng Kung University, Tainan, Taiwan, ROC.*

INTRODUCTION

Laser quenching is a heat treatment used to surface harden alloys such as martensitic-ferritic materials, carbon silicon, and Ti6Al4V (Hongwei et al., 2010; Cho et al., 2001; Fakir et al., 2018). In this research, a rotating cylindrical workpiece is heated by a gaussian laser and cooled by surface water cooling to calculate residual stress and corrosion resistance. The research applies this process to surface harden AISI 1000 & 4000 series steels and conduct thermal shock testing of SiC composites as shown in Fig. 1 (Hongwei et al., 2010; Fakir et al., 2018; Kim et al., 2017; Huang et al., 2012). Carbon steels like AISI 1000 & 4000 series are commonly used for gear tools, crankshafts, and linkages in automobiles and motorbikes after thermal hardening processing (Huang et al., 2012). CVD-SiC (chemical vapor deposited–silicon carbide) is an ideal material for advanced thermal processing of semiconductors and fuel cladding of nuclear power plants due to its high value of thermal conductivity, flexural strength, low thermal expansion coefficient like silicon, and excellent resistance to thermal shock, oxidation, and chemicals (Goela, et al., 2001). According to Daejong Kim & Donghee Lee et al. (2017), the thermal shock testing can be used to evaluate the thermal shock resistance by the high-temperature quenching process. Therefore, thermal fatigue failure of CVD-SiC, $Fe_{12}Cr_2Si$, and T91 alloys materials during the thermal shock testing is necessary research for the current design of fuel cladding.

Ji Li and Xikou He et al. (2022) mentioned the corrosion resistance of T91 fuel cladding can be evaluated by silicon concentration and thickness of the oxide layer. The parabolic rate constants formula is used to calculate the oxidation film thickness. However, Jeongyoun et al. (2006) said the silicon concentration can't perform the effective oxide film on the coolant pipe surface when the concentration is lower than 1.25 wt%. Therefore, both oxide film thickness and silicon concentration of $Fe_{12}Cr_2Si$ are referred to as the corrosion resistance from LBE.

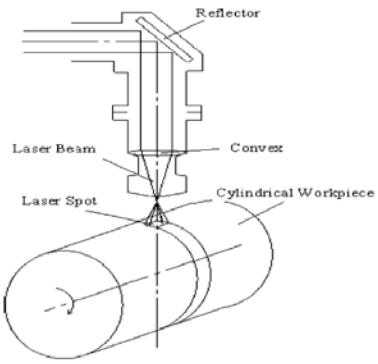

Fig. 1 Laser quenching of a cylindrical workpiece (Hongwei et al., 2010)

Thermal fatigue is widely recognized as an important potential damage mechanism in piping systems of nuclear power reactors (Kang, et al., 1999; Faidy et al., 2005; Paffumi et al., 2008). Although thermal fatigue is a well-known problem, much work is still needed to develop reliable predictive engineering approaches. The corrosion and thermal resistance for the pipe structures should be evaluated in the thermal shock testing environment.

This study evaluates the structure of nuclear coolant pipes made with FGC and FGM. The traditional FGC structure is made with T91 ferritic-martensitic alloys and $Fe_{12}Cr_2Si$ solid solutions (Ballinger et al., 2011; Ballinger et al., 2013), with LBE liquid as the cooling source for nuclear power. T91 alloys are used as the substrate metal of the model when Fe-Cr-Si solid solution is used as the surface corrosion-resisting coating. The working environment temperature of light water reactors (LWR) is about 250°C to 700°C (Ballinger et al., 2011; Ballinger et al., 2013; Serrano et al., 2013; Jeongyoun et al., 2006), while the LBE in nuclear coolant pipes is about 250°C to 500°C (Wenxuan et al., 2016; Hao et al., 2021). The Large-Break Loss-of-Coolant Accident (LBLOCA) is considered the worst scenario of nuclear power failure, with temperatures that could rise to 1200°C and cause the cladding wall fatigue failure (Kwangwon et al., 2018; Ting et al., 2019; Masahide et al., 2020). Due to the high-temperature conditions of nuclear power plants, thermal stress measurement and corrosion testing are necessary considerations (Vincenzo et al., 2010; Short et al., 2013; Huihua et al., 2018; Zhang et al., 2018). The maximum shear stress analysis is the main measurement for the residual stress of FGC and FGM structure. The FGC structure is made by CVD-SiC-$Fe_{12}Cr_2Si$ and T91-$Fe_{12}Cr_2Si$ components.

FGMs and material-property estimation approaches

Nowadays, the research of coolant pipes applied in nuclear power plants focuses on corrosion and oxidation resistance (Serrano et al., 2013; Jeongyoun et al., 2006; Wenxuan et al., 2016; Masahide et al., 2020; Short et al., 2013); however, the traditional welding structure of FGC may cause stress concentration and shorten the life of the system. In this study, Fick's law for diffusion equation is applied to the silicon concentration evaluation of $Fe_{12}Cr_2Si$ films; residual stress distribution is from the high-temperature environments.

The FGM mixture is based on the linear rule of mixture method (Huihua et al., 2018; Zhang et al., 2018; Zhou rt al., 2003; Cho et al., 2001); according to the linear rule of mixtures, any material property at a point location in dual-phase materials is approximated by a linear combination of volume fractions and individual material properties of two different materials can be described as below,

$$V_m(y) = [(d_G - y)\,/2\,d_G]^N$$
$$V_c(y) = 1 - V_m(y) \tag{1}$$

V_m: First-phase volume fraction, V_c: second-phase volume fraction, d_G: distance, N: non-negative real numbers. The real composition distribution of Eq. (1) is shown in Fig. 2. The volume fraction distribution can be depicted Fig. 3. When the real number is bigger than one, V_m varies urgently and transforms into another material slowly. On the other hand, when the real number is smaller than one, V_m transformed to V_c slowly in the front part and changed from M material to C material urgently. In this study, the N volume mixture number is ranged from 1/3 to 7 (i.e. 1/3、1/2、1、2、3…) to evaluate the influence of physical characteristics by different N. the main volume mixture number calculated in this research are 1/3、1/2、1、2、3. The oxide layer enhancement will be evaluated from 1/3 to 7. The initial concentration and diffusion coefficient can be taken as (Huihua et al., 2018; Zhang et al., 2018),

$$C(x) = V_m\,C_m + V_c C_c$$
$$D(\,x) = V_m\,D_m + V_c D_c \tag{2}$$

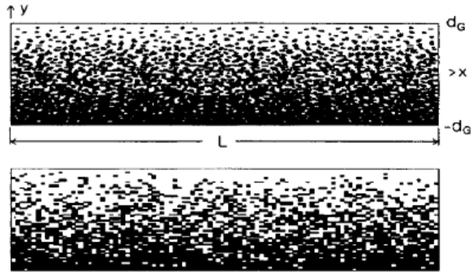

Fig. 2 an illustrative example of real composition distribution (Cho et al., 2001)

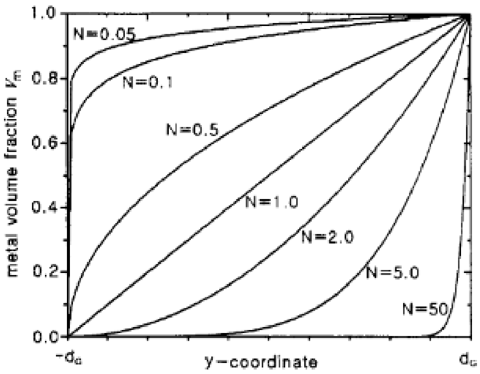

Fig. 3 the volume-fraction distributions (Cho et al., 2001)

The thermomechanical properties of dual-phase FGM have been estimated through several approaches; Cho et al. (2001) calculated the linear rule of the mixture and the Wakashima-Tsukamoto estimate compared to the discretized model, which indicates that the accuracy of the second numerical method is higher than the first approach. According to the Wakashima-Tsukamoto estimate, the averaged bulk modulus K is described as,

$$K = K_m + \frac{aV_c K_m (K_c - K_m)}{V_m K_c + aV_c K_m}\ ,$$
$$a = K_c(3K_m + 4\mu_m)/K_m(3K + 4\mu_c) \tag{3}$$

Then the shear modulus μ can be calculated by bulk modulus,

$$\mu = \mu_m + \frac{bV_c\mu_m(\mu_c - \mu_m)}{V_m\mu_c + bV_c\mu_m}\ ,$$
$$b = \mu_c(1+e)/(\mu_m + e\mu_c)\ ,$$
$$e = (9K_m + 8\mu_m)/(6K_m + 12\mu_m) \tag{4}$$

The elastic modulus E is calculated as,

$$E = 9K\mu/(3K + \mu) \tag{5}$$

Poisson's ratioυ can be calculated by bulk modulus and shear modulus,

$$v = (3K - 2\mu)/[2(3K + \mu)] \tag{6}$$

The thermal expansion coefficient α is,

$$\alpha = \alpha_m + \frac{(\frac{1}{K} - \frac{1}{K_m})(\alpha_c - \alpha_m)}{\frac{1}{K_c} - \frac{1}{K_m}} \tag{7}$$

Both thermal conductivity k and specific heat c can be described by linear rule of mixture,

$$k = V_m \cdot k_m + (1 - V_m) \cdot k_c \tag{8}$$
$$c = V_m \cdot c_m + (1 - V_m) \cdot c_c \tag{9}$$

In this research, $Fe_{12}Cr_2Si$, T91 and CVD-SiC alloys are the essential materials for the FGM structure. The design of FGM is based on the FGC structure, which comprises $Fe_{12}Cr_2Si$ and T91/CVD-SiC alloys; the FGM is classified as a two-phase FGM. The two-phase material is $Fe_{12}Cr_2Si$-T91, which varies from $Fe_{12}Cr_2Si$ to T91/CVD-SiC continuously. These processes can be depicted by Eq. (1).

The physical properties of $Fe_{12}Cr_2Si$, T91 alloys, and LBE are listed in Table 1. The elastic modulus of T91 alloys changes with the temperature; the variation between elastic modulus and temperature can be depicted as follows (Short et al., 2019),

$$\begin{aligned} &E[\text{Mpa}]=207300-64.58T[°C] \quad 20°C \le T \le 500°C \\ &E[\text{Mpa}]=295000-240T[°C] \quad 500°C \le T \end{aligned} \tag{10}$$

The thermal conductivity and specific heat of T91 are also varied by temperature. the variation between those parameters and temperature can be depicted in Eq. (11) and Eq. (12), respectively (Raju et al., 2015),

$$k_{T91}[W/m\cdot K] = 7.98 - 4.5\cdot 10^{-2}T + 1.02\cdot 10^{-4}T^2 - 1.14\cdot 10^{-7}T^3 + 6.38\cdot 10^{-11}T^4 - 1.42\cdot 10^{-14}T^5 \tag{11}$$

$$c_{T91}[J/kg\cdot K] = 9.78\cdot 10^4 - 1.69\cdot 10^2 T - 4.19\cdot 10^{-1}T^2 + 1.33\cdot 10^{-3}T^3 - 1.21\cdot 10^{-6}T^4 + 3.67\cdot 10^{-10}T^5 \tag{12}$$

The relation between temperature and thermal properties of $Fe_{12}Cr_2Si$ can be determined by experiments (Short et al., 2019; Raju et al., 2015). In this study, the curve fittings for thermal conductivity and specific heat are linear regressions shown in Eq. (13) and Eq. (14). The mechanical properties of elastic modulus、poisson's ratio、thermal expansion and bulk modulus are indicated in Table. 1 (Raju et al., 2015; Wang et al., 2017; Tao et al., 2019; Hosemann et al., 2010; Goela et al., 2001; Zhou et al., 2002).

$$k_{fe}[W/m\cdot K] = 9\cdot 10^{-11}\,T + 5.525\cdot 10^{-8} \tag{13}$$
$$c_{fe}[J/kg\cdot K] = 1.1877\,T + 8.871\cdot 10^{-1} \tag{14}$$

Table. 1 Mechanical properties (Raju et al., 2015; Wang et al., 2017; Tao et al., 2019; Hosemann et al., 2010; Goela et al., 2001)

	Elastic modulus	Poisson ratio	Thermal expansion	Bulk modulus
$Fe_{12}Cr_2Si$	216.4 (GPa)	0.31	5.2E-5 (1/K)	1.89E+11
T91	---	0.27	13E-6 (1/K)	1.73E+11
LBE	92.8 (MPa)	0.49	1.285E-04 (1/K)	3.093E+10
SiC	410 (GPa)	0.14	4E-06 (1/K)	1.76 E+11

(i) Safety margin analysis and maximum shear stress theory

Kwangwon et al. (2018) analyzed the stress distribution of nuclear power cladding based on the temperature variation during a significant break loss-of-coolant accident and calculated the margin of safety in Eq.17. The conclusion shows that the SiC can increase the cladding's margin of safety by15.68%-16.14% compared to Zry-4. The highest margin of safety is about 95%-98% based on this result. The margin of safety for the rotating tube in this study is evaluated to ensure that the value is higher than 98%; both safety factors and margin of safety are depicted as follows,

F.S.=ultimate load/allowable load (15)

M.O.S. =F.S. - 1.0 (16)

According to the maximum shear stress theory, it could be used for the evaluation of cladding strength,

$$\tau_{max} = max(|\sigma_1 - \sigma_2|, |\sigma_1 - \sigma_3|, |\sigma_2 - \sigma_3|) \quad (17)$$

σ_1, σ_2 and σ_3 are the three maximum principal stresses of the circular model respectively. In this research, the maximum shear stress should be lower than half of the yield strength and the margin of safety must be higher than 95%-98%.

(ii) The heat conduction equation and Thermal stress equation for rotating tube

In this study, pulsed laser is made by the high-power CO_2 laser. In Fig. 4, the 0th mode gauss laser distribution on a rotating cylindrical model for pulsed laser is shown. The experimental system includes a high-power 10.6 um 50 W CO_2 laser, an air-cooling system.

In this system, the infrared radiation pyrometer is used for detecting the outer surface temperature when the inner surface temperature is measured using thermocouple. The maximum shear stress is analyzed from the inner to outer surface. This laser power is based on 50 W CO_2 laser (coherent Inc. C-20 model, CW laser), the laser heat flux is depicted as below,

$$Q(r,z,t) = I_0(1-R)\, exp(-\frac{z}{\delta} - \frac{2r^2}{a^2}) \cdot f(t)/\delta \quad (18)$$

R is the reflective ratio of the pulsed laser energy, it’s described as $\frac{(n-1)^2+k^2}{(n+1)^2+k^2}$ when the CO_2 laser is heating on the coolant pipe surface vertically, n、k are the refractive index and the absorption coefficient respectively；I_0 is the maximum power intensity, which can be depicted as $\frac{2P}{\pi a^2}$. P is the power of pulsed laser；δ is called skin depth which can be calculated as $\frac{\lambda}{4\pi k}$. λ is the wavelength of the pulsed laser. Skin depth is used to describe the energy distinction of the material; f(t) is the pulse duration.

The heat conduction equation for 2D cylindrical model can be computed from transient heat flow,

$$\frac{1}{r}\frac{\partial}{\partial r}\left(kr\frac{\partial T}{\partial r}\right) + \frac{1}{r^2}\frac{\partial}{\partial \theta}\left(k\frac{\partial T}{\partial \theta}\right) + Q(r,\theta,t) = \rho c\frac{\partial T}{\partial t}, \; r_i<r<r_o, \; 0<\theta<\frac{\pi}{2} \quad (19)$$

$Q(r,\theta,t)$ is transformed by $Q(r,z,t)$ from Eq. (18), as the volumetric heat generation (W/m^2). In this research, the power P is assumed as 2E+08 W making the outer wall surface is heated to the maximum temperature 1200˚C.

The boundary condition of equation (20) is shown as,

$$B.C.\begin{cases} k\left.\frac{\partial T}{\partial r}\right|_{r=r_i} = 0 \\ k\left.\frac{\partial T}{\partial r}\right|_{r=r_o} = 2000 \end{cases} \quad (20)$$

In condition of the skin depth effect of pulsed laser, the power absorption of circular model is depicted on the radial direction. The value of z from Eq. (18) can be calculated as $r_o - r$, r_o is the outer radius. The heat flux from equation (20) is assumed as insulated on the inner radius because of the LBE liquid convective effect.

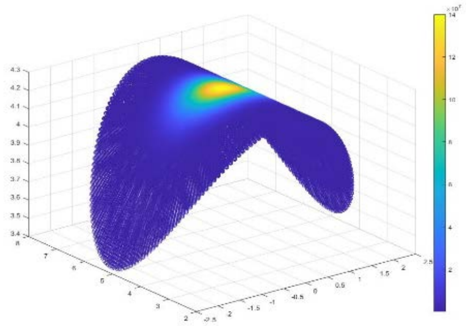

Fig. 4 0th mode gauss laser distribution on the rotating cylinder

According to recent studies about corrosion tests on coolant pipes, the oxidation on the pipe surface expands due to the tremendous amount of tensile stress and shear stress when LBE imposes the hydrostatic pressure on it. The higher shear stress caused by the turbulence from LBE on the pipe's surface may also increase corrosion invasion.

The force equilibrium in the radial direction is based on Kwangwon et al. (2018),

$$\frac{d\sigma_{rr}}{dr} + \frac{\sigma_{rr}-\sigma_{\theta\theta}}{r} = 0 \quad (21)$$

Hook's law,

$$\varepsilon^e_{rr} = \frac{1}{E}[\sigma_{rr} - \nu(\sigma_{\theta\theta} + \sigma_{zz})] \quad (22)$$

$$\varepsilon^e_{\theta\theta} = \frac{1}{E}[\sigma_{\theta\theta} - \nu(\sigma_{rr} + \sigma_{zz})] \quad (23)$$

$$\varepsilon^e_{zz} = \frac{1}{E}[\sigma_{zz} - \nu(\sigma_{\theta\theta} + \sigma_{rr})] \quad (24)$$

Strain-displacement relationships for plane strain condition,

$$\varepsilon^e_{\theta\theta} = \frac{u}{r} - \alpha \cdot T \quad (25)$$

$$\varepsilon^e_{rr} = \frac{\partial u}{\partial r} - \alpha \cdot T \quad (26)$$

$$\varepsilon^e_{zz} = -\alpha \cdot T \quad (27)$$

where σ_{rr} and $\sigma_{\theta\theta}$ are the radial and hoop stress components respectively; for the thick hollow cylinder, σ_{rr} and $\sigma_{\theta\theta}$ are given in terms of the radial displacement u by,

$$\sigma_{rr} = \left[A_{11}\frac{\partial u}{\partial r} + A_{12}\frac{u}{r} + A_{13}\alpha \cdot T\right] \cdot E \quad (28)$$

$$\sigma_{\theta\theta} = \left[A_{12}\frac{\partial u}{\partial r} + A_{11}\frac{u}{r} + A_{13}\alpha \cdot T\right] \cdot E \quad (29)$$

$$\sigma_{zz} = -\alpha T \cdot E + \nu(\sigma_{rr} + \sigma_{\theta\theta}) \quad (30)$$

For plane strain condition, E is the modulus of elasticity and A_{11}, A_{12} and A_{13} are related to Poisson's ratio ν as,

$$A_{11} = \frac{1-\nu}{(1+\nu)(1-2\nu)} \quad (31)$$

$$A_{12} = \frac{\nu}{(1+\nu)(1-2\nu)} \quad (32)$$

$$A_{13} = \frac{-1}{1-2\nu} \quad (33)$$

The substitution of equations (28) and (29) for Eq. (21) produces the Navier equation,

$$\frac{\partial^2 u}{\partial r^2} + \left(\frac{1}{E}\frac{\partial E}{\partial r} + \frac{1}{r}\right)\frac{\partial u}{\partial r} + \left(\frac{A_{12}}{A_{11}E\cdot r}\cdot\frac{\partial E}{\partial r} - \frac{1}{r^2}\right)u = -\frac{A_{13}}{A_{11}E}\frac{\partial(E\cdot\alpha T)}{\partial r} \quad (34)$$

A schematic of the 3D part is shown in Fig. 5 (a). Since (σ_{rr}, $\sigma_{\theta\theta}$, σ_{zz}) are the primary principal stresses, the Tresca theory is depicted by Eq. (17),

$$\tau_{max} = max(|\sigma_{rr} - \sigma_{\theta\theta}|, |\sigma_{rr} - \sigma_{zz}|, |\sigma_{\theta\theta} - \sigma_{zz}|) \quad (35)$$

The mesh element for the rotating cylindrical model is an 10-node tetragonal element. There are three translational degrees of freedom at each node, viz. in this study, the model will keep rotating until the outer surface is heating above 1200 ˚C, the model is shown in Fig. 5(a).

On the other hand, the 2D finite element in Fig. 5(b) is used as the evaluation of corrosion resistance. It's component of 2D quadrilateral 8-node element. The gaussian laser boundary is set on the outer wall of the cylindrical model.

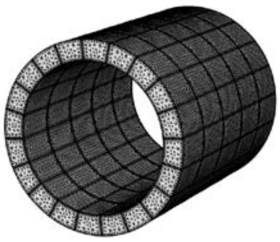

Fig. 5(a) Schematic of 3D finite element part with the Gaussian laser boundary condition

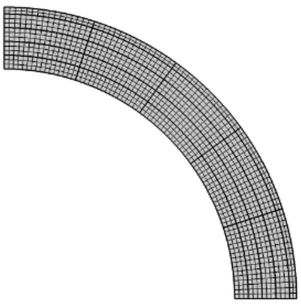

Fig. 5(b) Schematic of 2D finite element part with the Gaussian laser boundary condition

(iii) Tamura-Tomota-Ozawa (TTO) model

The TTO model assumes that the magnitude of stress and strain on every area of two-phase FGM material is dependent on stress and strain of phase constituents undergone with their volume fractions as given (Woo et al., 2017; Vasavi et al., 2021),

$$\sigma = \sigma_1 V_1 + \sigma_2 V_2$$
$$\varepsilon = \varepsilon_1 V_1 + \varepsilon_2 V_2 \quad (36)$$

Where σ and ε represent the stresses and strains on every region of a two-phase FGM with various volume fractions of V_1 and V_2, this model can determine the yield strength of FGMs as given in Eq. (1), such as elastic modulus and thermal expansion coefficient,

$$\sigma_y = \sigma_{y1}\left[V_1 + \left(\frac{q+E_1}{q+E_2}\right)\left(\frac{E_2}{E_1}\right)(1-V_1)\right] \quad (37)$$

σ_{y1} is the yield strength of phase 1 material. Here q indicates the stress to strain ratio that depends on material types and micro-structural interactions among the two phases. It is calculated based on the distribution of the yield strength of two-phase conditions like Fig. 6.

According to the yield strength-temperature relation of T91 alloys and $Fe_{12}Cr_2Si$ solid solutions (Jeongyoun et al., 2006), the yield strength at different temperatures varying from 700 ˚C to 1200 ˚C is calculated through the curve fitting of the data from the tensile strength experiment. The yield strength of CVD-SiC is based on the materials engineering handbook. The silicon carbide is supposed as the ceramic structure with the room temperature (Shackelford et al., 2015).

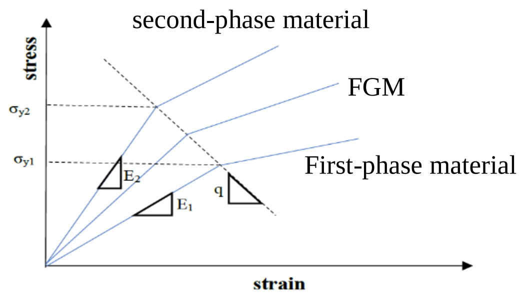

Fig. 6 The stress vs. strain curve of an arbitrary two-phase FGM (E_1: First-phase material, E_2: Second-phase material)

(iv) The diffusion boundary conditions for the evaluation of corrosion testing.

The silicon concentration moves from regions of high concentrations to the low concentration place at a rate proportional to the concentration gradient. Fick's law was applied to depict this diffusive flux in multiple dimensions mathematically (Samel et al., 2005),

$$\frac{\partial c}{\partial t} = \nabla\cdot(D\,\nabla\cdot c) \quad (38)$$

c(x,t) function is the concentration function which varies based on different regions and time steps; D (m^2/s) is the diffusion coefficient, which is described as an Arrhenius-based diffusion coefficient (Jeongyoun et al., 2006),

$$D = D_0\, exp(-E_A/RT)\ \left[\frac{m^2}{sec}\right] \quad (39)$$

where D_0 is the temperature-independent diffusion constant, E_A is the activation energy of the process in J/mol, R is the universal gas constant (8.314 J/mol-K), and T is the absolute temperature in Kelvin. Ballinger et al. (2013) wrote the program of minimum mean squared error (MSE) in C to fit the diffusion coefficient for silicon in BCC T91/F91 alloys,

$$D_{si\ in\ bcc\ \mathrm{T91}} = 5 \times 10^{-3}\, exp(-253969/RT)\ [\frac{m^2}{sec}] \tag{40}$$

The silicon diffusion coefficient in $Fe_{12}Cr_2Si$ can be roughly estimated through $D_{si}=10^{-14} m^2/s$ at high temperatures in the $Fe_{12}Cr_2Si/Cr$ interfacial region aged experiment (Short et al., 2019).

On the other hand, the silicon diffusion coefficient of CVD-SiC in this study is analyzed by the linear curve fitting, the discretized data comes from the chemical analyses of β-silicon carbide in the high temperature environment range from 1800K to 2300K (Datta et al., 2002). The initial silicon concentration in silicon-carbide is based on the stabled condition of SiC PWR (pressured water reactor) (Shackelford et al., 2015), which is about 0.18 wt.%.

In this research, the 2D finite element model is tubular cross-sections; the cylindrical coordinates (r,θ,z), the diffusion process of Eq. (38) is described by the classical diffusion equation for cylindrical coordinates,

$$\frac{\partial c}{\partial t} = \frac{1}{r}\left(\frac{\partial}{\partial r}\left(r \cdot D\frac{\partial c}{\partial r}\right) + \frac{\partial}{\partial \theta}\left(\frac{D}{r}\frac{\partial c}{\partial \theta}\right)\right) \tag{41}$$

When the LBE goes through the inner wall of the coolant pipe, the silicon diffusion coefficient of LBE can be estimated by first principles molecular dynamics (FPMD), which is about 3.8×10^{-5} m^2/s. This system can be performed in a pure LBE systems to evaluate the diffusion coefficient of silicon atoms (Wenyi et al., 2019).

The Finite element approach using a two-dimensional transient problem has been developed with Eq. (41) to analyze the diffusion condition of the FGM and FGC structures in the dynamic temperature environment.

The temperature verification during the rotating process

In this research, thermal quenching testing is used to simulate the quenching process. The temperature of the cylindrical model is raised to about 1700K and then rapidly reduced to room temperature (293.15K) through rotation. The convection coefficient of 2000 W/mK is obtained from the LBE boundary equation (Eq. 20). The outer surface of the model is dynamically heated by a Gaussian beam laser. The temperature validation of the AISI 1040 model during thermal shock testing is presented in Figs. 7(a), 8(a), and 9(a), respectively.

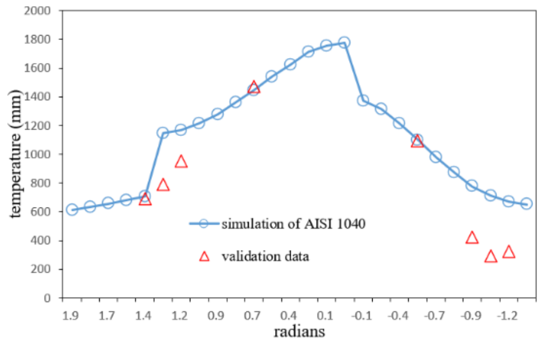

Fig. 7(a) Temperature field variation on the surface with time (t=0.5s) (Hongwei et al., 2010)

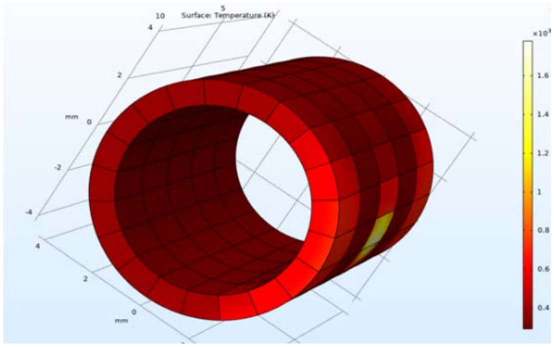
Fig. 7(b) Temperature field variation with time (t=0.5s)

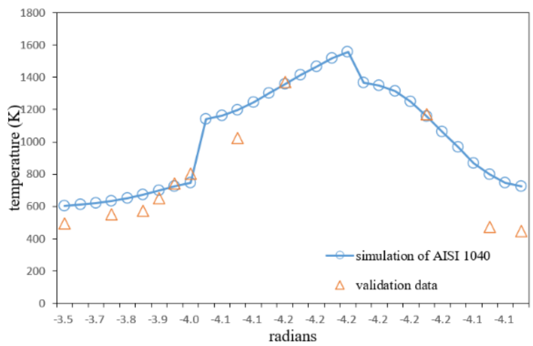

Fig. 8(a) Temperature field variation on the surface with time (t=1s) (Hongwei et al., 2010)

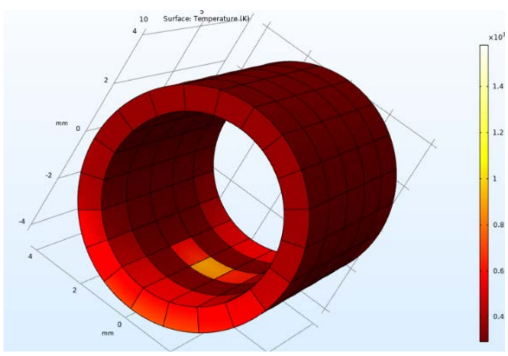
Fig. 8(b) Temperature field variation with time (t=1s)

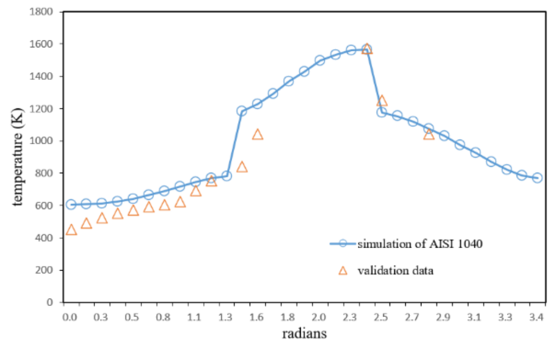

Fig. 9(a) Temperature field variation on the surface with time (t=1.7s) (Hongwei et al., 2010)

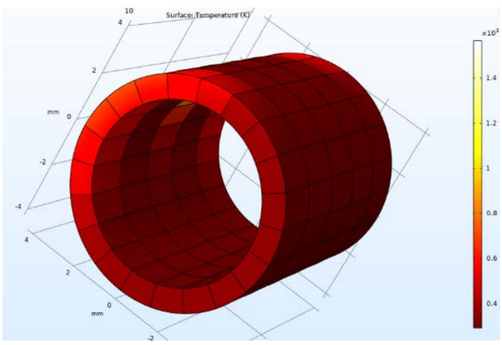

Fig. 9(b) Temperature field variation with time (t=1.7s)

The residual stress evaluation of FGC & FGM structure

The residual stress after the thermal quenching process is analyzed by investigating the deformation of the FGC/FGM structure caused by the temperature rise, which can be attributed to the release of residual stress on the cutting surface (Masoudi et al., 2015). The results of the $Fe_{12}Cr_2Si$-T91 and $Fe_{12}Cr_2Si$-SiC FGC models are presented in Figs. 10 and 11, respectively. The stress is distributed from the inner wall to the outer wall, specifically from a radius of 3.35 mm to 4.25 mm. In the $Fe_{12}Cr_2Si$-T91 FGC model, the residual stress indicates a yield strength higher than the tresca stress. However, the lowest safety margin observed is only 0.268, as shown in Fig. 12, which is less than 0.98.

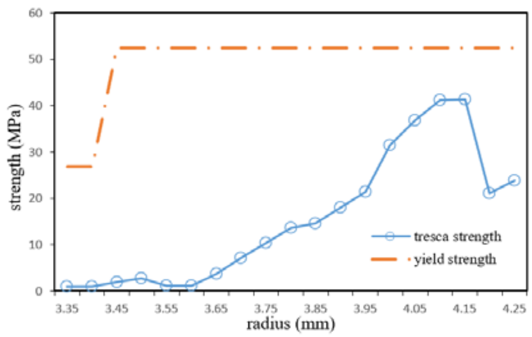

Fig. 10 Residual stress of FGC $Fe_{12}Cr_2Si$:T91 (tresca stress)

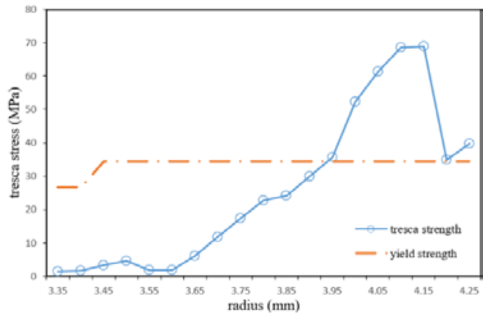

Fig. 11 Residual stress of FGC $Fe_{12}Cr_2Si$:SiC (tresca stress)

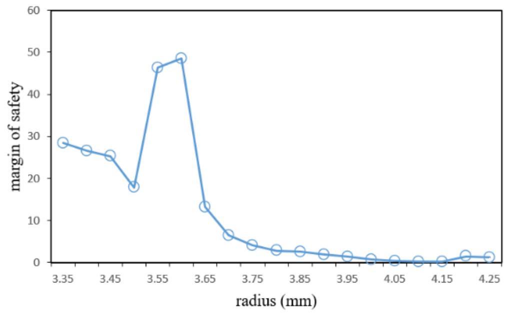

Fig. 12 Safety margin of $Fe_{12}Cr_2Si$:T91(FGC)

This may pose a problem for traditional FGC $Fe_{12}Cr_2Si$-T91 structures under LBLOCA conditions. On the other hand, the yield strength is lower than the tresca stress for the rotating model formed by the $Fe_{12}Cr_2Si$-SiC FGC structure, as shown in Fig. 11. These results suggest that the FGC models of $Fe_{12}Cr_2Si$-T91 and $Fe_{12}Cr_2Si$-SiC construction may not be ideal structures for use in high-temperature environments.

In this study, the FGM model is considered as a potential solution to increase the margin of safety against residual stress due to its continuous material distribution. The tresca stress of the $Fe_{12}Cr_2Si$-T91 and $Fe_{12}Cr_2Si$-SiC FGM models are presented in Figs. 13 and 15, respectively. Fig. 16 shows that increasing the exponential number of the $Fe_{12}Cr_2Si$-T91 volume mixture can enhance the margin of safety. However, the margin of safety seems too large for this structure in the radius range of approximately 3.55 to 3.95 mm, which may result in material waste.

The performance of the $Fe_{12}Cr_2Si$-SiC FGM model is evaluated in Fig. 15. It is observed that increasing the exponential number of the volume mixture improves the margin of safety effectively. However, the margin of safety becomes positive when the exponential number of volume mixture exceeds N=2. This suggests that a higher exponent number is necessary when the material component is formed by the $Fe_{12}Cr_2Si$-SiC structure. For the $Fe_{12}Cr_2Si$-SiC FGM model, the margin of safety for N=3 ranges from 14.031 to 2881.95, which is more reasonable than the margin of safety for the $Fe_{12}Cr_2Si$-T91 structure shown in Fig. 14 and reduces the material cost. The enhancement percentage of the margin of safety due to the $Fe_{12}Cr_2Si$-SiC FGM model is evaluated in Fig. 17, which compares the $Fe_{12}Cr_2Si$-T91 FGC and $Fe_{12}Cr_2Si$-SiC FGM models. The enhancement ranges from 930.5% to 13363.3%. The strength of the inner wall is improved effectively with N=3. The volume fraction of SiC is about 88.36% when the radius location is 4.15 mm on the cylindrical tube. This condition results in a much higher yield strength of the FGM model than the tresca stress, inevitably increasing the safety margin.

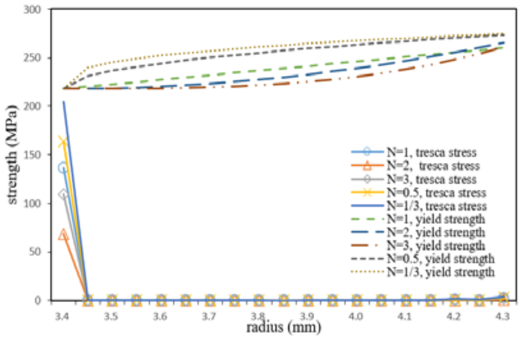

Fig. 13 Residual stress of FGM $Fe_{12}Cr_2Si$: T91(unit: MPa)

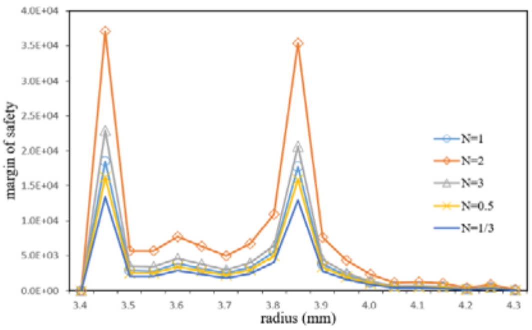

Fig. 14 Safety margin of FGM $Fe_{12}Cr_2Si$: T91

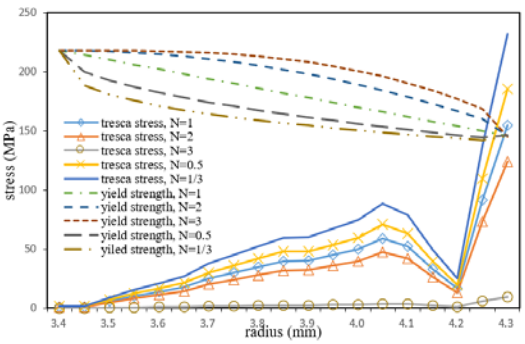

Fig. 15 Residual stress of FGM $Fe_{12}Cr_2Si$: SiC (unit : MPa)

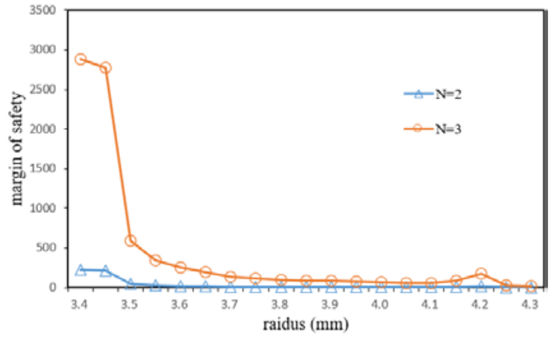

Fig. 16 Safety margin of FGM $Fe_{12}Cr_2Si$: SiC

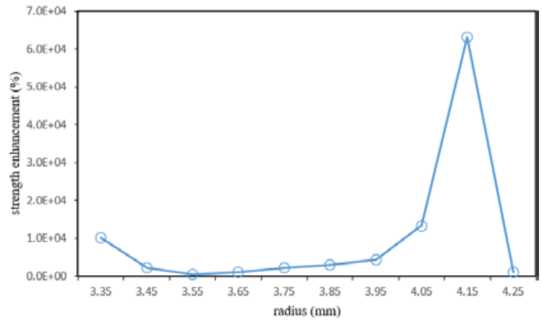

Fig. 17 The enhancement of margin of safety (FGM $Fe_{12}Cr_2Si$-SiC & FGC $Fe_{12}Cr_2Si$:T91)

Corrosion resistance and oxide layer evaluation

The silicon concentration on the inner surface of the 2D circular model is an important factor in evaluating corrosion resistance. The diffusion coefficient of T91 alloys and silicon carbide varies with temperature, as shown in Equation (40). To simulate a high-temperature environment at 1200°C, a thermal shock boundary is applied to the outer wall, and the time range is from 0 to 10E+04 hours. This allows for the observation of the detailed variation of silicon concentration and the growth of the oxide layer formed by silicon and oxygen on the inner wall.

In summary, the corrosion resistance of $Fe_{12}Cr_2Si$-T91 and $Fe_{12}Cr_2Si$-SiC FGC models was evaluated by simulating the diffusion of silicon concentration on the inner surface of a 2D circular model was obtained and compared with that obtained using any commercial package. The growth of the oxide layer formed by silicon and oxygen on the inner wall was observed by testing the thermal shock boundary on the outer wall, ranging from 0 to 10E+04 hours. The thickness of the oxide layer was calculated using Equation (42), where ΔX is the oxide thickness in micrometers, kp is the parabolic rate constant in $\mu m^2/h$, and t is the time in hours. The parabolic rate constant was determined from different silicon concentrations shown in Table 2 (Li et al., 2022), which were stable after approximately 10 hours. The verified model of LBE wettability test was based on the experiment by Li et al. (2022), where LBE droplets were deposited on a T91 sheet sample to observe the oxide layer growth. The simulation of the 30×10×2 mm^3 $Fe_{12}Cr_2Si$-T91 and $Fe_{12}Cr_2Si$-SiC FGC finite element models within the same diffusion boundary of the wettability test was compared to the experiment result from Fig 18. The oxide layer growth rate of $Fe_{12}Cr_2Si$-T91 and $Fe_{12}Cr_2Si$-SiC FGC structure ranged from 0 to 1000 hours was lower than T91LSi when it's higher than T91MSi and T91HSi. The oxidized layer on the $Fe_{12}Cr_2Si$ surface of FGC model was calculated by the silicon concentration and shown in Fig 19. The results showed that the oxidized layer of $Fe_{12}Cr_2Si$-T91 structure grows faster than $Fe_{12}Cr_2Si$-SiC for FGC model when the diffusive time arrives 1E+04 hours.

$$\Delta X^2 = k_p t \tag{42}$$

Table 2 parabolic rate variation with silicon concentration (Li et al., 2022)

Silicon concentration	Parabolic rate constants (μ m^2/h)
0.48(wt%)	1.1253
1.30(wt%)	0.8442
1.95(wt%)	0.7114

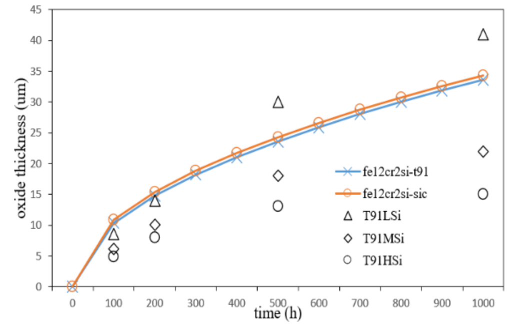

Fig. 18 Oxidized layer growth on FGC sample (unit: um) (He et al., 2022)

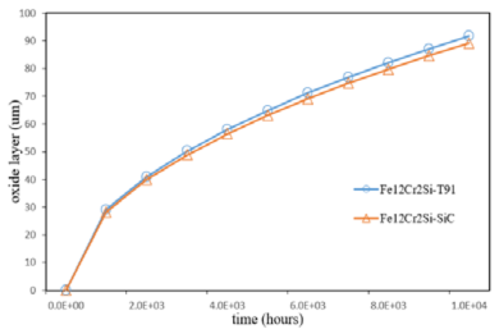

Fig. 19 Oxidized layer of FGC (unit: um)

To summarize, the $Fe_{12}Cr_2Si$-SiC FGM model exhibits improved corrosion resistance compared to the $Fe_{12}Cr_2Si$-T91 FGC model, especially when the volume mixture number is increased. In the $Fe_{12}Cr_2Si$-T91 FGM model, the oxide layer growth rate is higher when the volume mixture number is lower, while in the Fe12Cr2Si-SiC FGM model, the oxide layer growth rate is promoted when the volume mixture number is higher. Those results are shown in Fig. 20 and Fig. 21, respectively. This is because the silicon concentration in $Fe_{12}Cr_2Si$ gradually replaces the silicon concentration in T91 alloys in the $Fe_{12}Cr_2Si$-T91 FGM model, resulting in faster oxide layer growth. However, in the $Fe_{12}Cr_2Si$-SiC FGM model, the oxide layer growth rate is increased due to the immediate descent of silicon concentration on the outer wall. In conclusion, the $Fe_{12}Cr_2Si$-SiC FGM model is an ideal design for fuel cladding structures, especially when the volume mixture number is increasing.

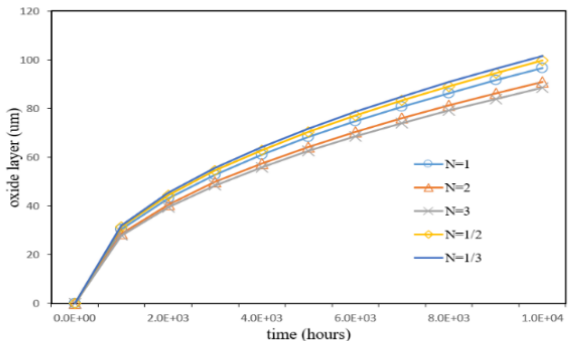

Fig. 20 Oxidized layer of $Fe_{12}Cr_2Si$: T91 FGM (unit: um)

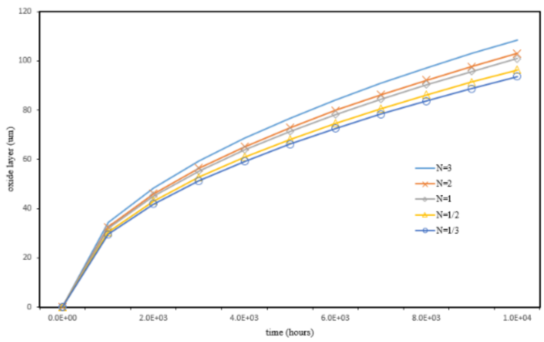

Fig. 21 Oxidized layer of $Fe_{12}Cr_2Si$:SiC FGM (unit: um)

In summary, the $Fe_{12}Cr_2Si$-SiC FGM model can be an ideal design for fuel cladding structures. As the volume mixture real number increases, the oxide layer growth enhancement compared to the traditional $Fe_{12}Cr_2Si$-T91 FGC model is shown in Fig. 22. The thickness of the oxide layer increases as the volume fraction rises. This increase in oxide thickness on the inner wall surface can effectively improve corrosive resistance (Li et al., 2022). The volume increase of SiC facilitates the urgent flow of silicon concentration on the inner surface to the substance material. As a result, the parabolic rate constant rises, which leads to an improvement in corrosive resistance.

When the volume fraction of the $Fe_{12}Cr_2Si$ -SiC FGM model is less than one, the oxide thickness on the inner wall of fuel cladding increases slowly compared to the traditional $Fe_{12}Cr_2Si$-T91 FGC model. However, as shown in Fig. 22, the enhancement rate is significantly promoted from 2.302% to 10.08% when the volume fraction is one, compared to the number of 2/3. The oxide thickness enhancement rate still gradually increases when the volume fraction exceeds one. This result also highlights how the improvement of the Fe-Cr-Si system can enhance the corrosive resistance to LBE liquid (Ballinger et al., 2011).

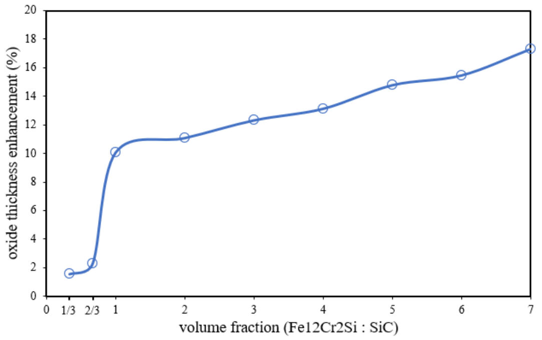

Fig. 22 the thickness enhancement of oxide layer at 10E+04 hours ($Fe_{12}Cr_2Si$:SiC FGM/ $Fe_{12}Cr_2Si$:T91 FGC)

Table. 3 the thickness enhancement of oxide layer at 10E+04 hours ($Fe_{12}Cr_2Si$: SiC FGM/ $Fe_{12}Cr_2Si$:T91 FGC)

100%	1/3	2/3	1	2	3	4	5
enhancement	1.56	2.302	10.08	11.08	12.32	13.13	14.78

Conclusion

In this study, the FGM model based on $Fe_{12}Cr_2Si$-T91/SiC material was investigated as a means of improving the margin of safety and corrosive resistance. Simulations were performed using FGC and FGM structures, with a Gaussian CO_2 laser heating the 3D rotating tube and 2D cylindrical model of working temperatures from 20°C to 1200°C. The tresca stress and silicon concentration of the $Fe_{12}Cr_2Si$ solid solution were characterized and examined. The key conclusions drawn in this study are given as follows:

1. The safety margin analysis of FGM model indicates the $Fe_{12}Cr_2Si$-SiC model can significantly improve the margin of safety as compared to the FGC model formed by $Fe_{12}Cr_2Si$-SiC. After the tube model rotating for five times, the temperature on the cylindrical model rises to 1200°C. The residual stress and margin of safety is evaluated at the temperature. The safety margin of traditional FGC model of $Fe_{12}Cr_2Si$-T91 is ranged from 0.268 to 28.52 when the FGM of $Fe_{12}Cr_2Si$-SiC model at N=3 has a higher safety margin from 14.031 to 2881.95. This result demonstrates that the FGM can effectively enhance the safety margin as compared to that of the FGC structure.
2. The FGM design is composed of a $Fe_{12}Cr_2Si$-T91/SiC structure, which has a safety margin of not much higher than 0.98 on the inner wall of the $Fe_{12}Cr_2Si$-T91 structure. This could lead to plastic deformation on the inner surface of the FGM tube model or cause the LBLOCA condition. However, changing the substance material from T91 alloys to SiC and increasing the volume mixture number to three (N=3) can improve the safety margin. The percentage increase in the safety margin close to the outer wall of the rotating tube can also be improved up to 6.0E+04% as compared to that of the traditional FGC model. This result indicates that the strength of the $Fe_{12}Cr_2Si$-SiC FGM structure can be enhanced in high-temperature environment by increasing the volume mixture number.
3. The oxidized layer growth of the FGC model shows that the $Fe_{12}Cr_2Si$-T91 structure forms a little faster than that of $Fe_{12}Cr_2Si$-SiC. The parabolic rate constant indicates that the decrease of silicon concentration can effectively improve the constant. This results in the oxidized layer on the surface of $Fe_{12}Cr_2Si$-T91 becoming thicker than that of Fe_{12}Cr2Si-SiC when the diffusive time reaches 1.0E+04 hours.
4. The growth ofoxidized thickness of the $Fe_{12}Cr_2Si$-SiC FGM model becomes faster when the volume fraction increases. In this study, we found that the $Fe_{12}Cr_2Si$-SiC FGM model structure with a volume fraction of 7 exhibits a higher oxide thickness than the traditional $Fe_{12}Cr_2Si$-T91 FGC model, as shown in Fig. 24. Specifically, at 1.E+04 hours, the oxide layer of the $Fe_{12}Cr_2Si$-SiC FGM model has been improved by a range from 1.56% to 17.31% as compared to that of the $Fe_{12}Cr_2Si$-T91 FGC model, especially for models with a volume fraction higher than one. Therefore, the $Fe_{12}Cr_2Si$-SiC FGM structure is an ideal design for fuel claddings and coolant pipes, particularly when considering the LBLOCA accident.

Reference

Ballinger R. G., (2011). "The development and production of a functionally graded composite for Pb-Bi service", U.S. Department of Energy Office of Scientific and Technical Information, (Technical Report DOE-ID1 4742).

Ballinger R. G., (2013). "Materials testing and development of functionally graded composite fuel cladding and piping for the lead-bismuth cooled nuclear reactor", Master's thesis, Massachusetts Institute of Technology, Massachusetts.

Bingsheng L., Qing L., & Hongpeng Z., (2021). "The effects of stress on corrosion behavior of SIMP martensitic steel in static liquid lead-bismuth eutectic", Corrosion Science, vol. 187, doi: 10.1016/j.corsci.2021.109477.

Cho J. R. & Ha D. Y., (2001). "Averaging and finite element discretization approaches in the numerical analysis of functionally graded materials", vol. 302, Iss. 2, pp. 187-196.

Datta. M. S., Bandyopadhyay. A. K., & Chaudhuri. B. (2002). Sintering of nano crystalline α silicon carbide by doping with boron carbide. *Bulletin of Materials Science*, *25*, 181-189.

Faidy, C., Chapuliot, S., & Mathet, E. (2005). Thermal Fatigue of Reactor Components in OECD-NEA Member Countries: a Three Fold Program to Enhance Cooperation.

Fakir, R., Barka, N., & Brousseau, J. (2018). Case study of laser hardening process applied to 4340 steel cylindrical specimens using simulation and experimental validation. *Case Studies in Thermal Engineering*, *11*, 15-25.

Goela, J. S., Brese, N. E., Burns, L. E., & Pickering, M. A. (2001, September). CVD-SiC for RTP chamber components. In *9th International Conference on Advanced Thermal Processing of Semiconductors, RTP 2001* (pp. 217-224). IEEE.

Hao W., Jun X., & Hui W., (2021). "Corrosion behavior and surface treatment of cladding materials used in high-temperature lead-bismuth eutectic alloy: a review", Coatings, vol. 11, Iss. 3, doi: 10.3390/coatings11030364

Huihua Z., Simin L., & Shangyu H., (2018). "The numerical manifold method for transient moisture diffusion in 2D functionally graded materials", IOP Conference Series. Earth and Environmental Science, vol. 189, Iss. 3, doi: 10.1088/1755-1315/189/3/032017.

Hongwei X., Wayne C. W., & Zhou K., (2010). "Temperature field computation for a rotating cylindrical workpiece under laser quenching", The International Journal of Advanced Manufacturing Technology, doi: 10.1007/s00170-009-2206-5.

Huang S. F., (2012). "Laser surface hardening of AISI 4140 steel. Journal of China University of Science and Technology", vol. 50, pp. 49-59.

Hosemann P., Kabra S., & Stergar E., (2010). "Micro-structural characterization of laboratory heats of the Ferric/Martensitic steels HT-9 and T91", Journal of Nuclear Materials, vol. 403, Iss. 1-3, pp. 7-14.

Jeongyoun L., (2006). "Effects of Chromium and silicon on corrosion of iron alloys in lead-bismuth eutectic", Ph.D. thesis, Massachusetts Institute of Technology, Massachusetts.

Joonho M., Sungyu K., & Won D. P., (2019). "Initial oxidation behavior of Fe-Cr-Si alloys in 1200℃ steam", Journal of Nuclear Materials, vol. 513, pp. 297-308

Kang, K. S., & Kupca, L. (1999). Assessment and Management of Ageing of Major Nuclear Power Plant Components Important to Safety: Steam Generators. Tech. Rep. TECDOC-1668, IAEA.

Kwangwon A., Kyohun J., & Sung P. P., (2018). "Safety evaluation of silicon carbide and zircaloy-4 cladding during a Large-Break Loss-of Coolant Accident", Energies, vol. 11, Iss. 12, doi: 10.3390/en11123324.

Kim, D., Lee, D., Lee, S., Park, K., Lee, H. G., Park, J. Y., & Kim, W. J. (2017). Thermal shock resistance and hoop strength of triplex silicon carbide composite tubes. *International Journal of Applied Ceramic Technology*, *14*(6), 1069-1076.

Li, J., He, X., Xu, B., Tang, Z., Fang, C., & Yang, G. (2022). Effect of Silicon on Dynamic/Static Corrosion Resistance of T91 in Lead–Bismuth Eutectic at 550° C. *Materials*, *15*(8), 2862.

Masahide S., Kenta M., & Takashi S., (2020). "Verification of safety margin of reactor pressure vessel exposed to various thermal transients based on probabilistic approach", E-Journal of Advanced Maintenance, vol. 11, No. 4, pp. 172-178, ISSN-1883-9894.

Masoudi, S., Amirian, G., Saeedi, E., & Ahmadi, M. (2015). The effect of quench-induced residual stresses on the distortion of machined thin-walled parts. *Journal of Materials Engineering and Performance*, *24*, 3933-3941.

Paffumi, E., Nilsson, K. F., & Taylor, N. G. (2008). Simulation of thermal fatigue damage in a 316L model pipe component. *International Journal of Pressure Vessels and Piping*, *85*(11), 798-813.

Postlethwaite J., & Nesic S., (1991). "Hydrodynamics of disturbed flow and erosion-corrosion. Part I-single-phase flow study", The Canadian Journal of Chemical Engineering, vol. 69, Iss. 3, pp. 698-703.

Raju S., Haraprasanna T., & Arun K. R., (2015). "Thermal expansion characteristics of Fe-9Cr-0.12C-0.56Mn-0.24V-1.38W-0.06Ta (wt%) reduced activation ferritic-martensitic steel", vol. 459, pp. 150-158.

Serrano De Caro, Magdalena, Woloshun, Keith A., Rubio, Floren V., & Maloy, Stuart A.. "Materials Selection for the Lead-Bismuth Corrosion and Erosion Tests in DELTA Loop". United States.

Short M. P., Ballinger R. G., & Hanninen H. E., (2013). "Corrosion resistance of alloys F91 and Fe-12Cr-2Si in lead-bismuth eutectic up to 715℃", Journal of Nuclear Materials, vol. 434, Iss. 1-3, pp. 259-281.

Short, Michael Philip, & McAlpine. *NEUP Final Report: Multilayer Composite Fuel Cladding and Core Internals for LWR Performance Enhancement and Severe Accident Tolerance*. United States. https: //doi.org/10.2172/1572872.

Samuel M. A., (2005). "Kinetics of materials", New Jersey: John Wiley & Sons.

Shackelford J. F., Han Y. H., & Kim S., (2015). "CRC Materials Science and Engineering Handbook", Boca Raton: CRC Press.

Ting W. L., (2019). "Risk-informed safety margin characterization for A Larger Break Loss-of-coolant Accident of Nuclear Power Plants and Associated Peak Cladding Temperature Margin Evolution", Master Thesis, University of Liverpool, Liverpool.

Tao W., Takashi N., & Masatoshi F., (2019). "Numerical study on the potential of cavitation damage in a lead-bismuth eutectic spallation target", Materials, vol. 12, Iss. 4, doi: 10.3390/ma12040681.

Tao W., & Shigeru S., (2018). "Flow-accelerated corrosion of type 316L stainless steel caused by turbulent lead-bismuth eutectic flow", Metals, doi: 10.3390/met8080627.

Vincenzo V. R., & Thierry W., (2010). "The high burn-up structure in nuclear fuel", materials today, vol. 13, Iss. 12, pp. 24-32.

Vasavi B., Raghavendra G., & Shakuntla O., (2021). "State of the art in functionally graded materials", Composite Structures, vol. 262.

Wenxuan X., Yongwei W., & Xunfeng L., (2016). "Experimental investigation of the thermal hydraulics in lead bismuth eutectic-helium experimental loop of an accelerator-driven system", Nuclear Engineering and Technology, vol. 48, Iss. 5, pp. 1154-1161.

Wang J., (2017). "Study of microstructure evolution in F/M steel T91 by in-situ synchrotron wide-angle X-rays scattering", Master Thesis, University of Illinois, Illinois.

Woo Y. J., & Sung C. H., (2017). "Analysis of functionally graded material plates using sigmoidal law", Mathematical Problems in Engineering, vol. 4, Iss. 8,

Wenyi D., Zhizhong J., & Jingping X., (2019). "Interactions between alloy elements and oxygen at the steel-liquid LBE interface determined from first-principles molecular dynamics simulations", Physical Chemistry Chemical Physics, Iss. 46, doi: 10.1039/c9cp05626b, pp. 25521-25926.

Zhang H., Liu S., & Han S., (2018). "Modelling steady moisture diffusion in functionally graded materials with the numerical manifold method", IOP Conference Series. Earth and Environmental Science, vol. 189, Iss. 4, doi: 10.1088/1755-1315/189/4/042018.

Zhou B., (2003). "The effect of the pre-existing surface crack morphologies on the thermal fracture of ceramic coatings", Ph.D. thesis, Purdue University, Indiana.

Zhou Y. C., Hashida. T, (2002). "Thermal fatigue failure induced by delamination in thermal barrier coating", International Journal of Fatigue, vol. 24, Iss. 2-4, pp. 407-417.

旋轉圓管熱焠火工藝應用於碳化矽與 T91 合金傳統功能複合材料與功能材料強化結構之抗熱強度與抗腐蝕提升

賴新一　羅凱謙
國立成功大學機械工程學系

摘要

CVD-碳化矽和 T91 馬氏體-鐵素體合金被廣泛認為是輕水型反應堆（LWR）的核燃料管道不可或缺之重要基材。由於在該材料高溫環境下具有優異的高溫和耐腐蝕性。本文旨在分別研究 CVD-碳化矽-$Fe_{12}Cr_2Si$ 和 T91-$Fe_{12}Cr_2Si$ 功能性梯度複合材料（FGC）和功能性梯度資料（FGM）。應用於具有雷射淬火邊界的 3D 旋轉圓柱結構與高溫致 1200℃的 2D 圓柱模型用以模擬在 20℃~1200℃環境中的核反應爐管道工作情形。

在本研究中，線性體積分率法與 Wakashima-Tsukamoto 演算法是 FGM 之主要演算法。FGM 材料的連續性分佈可以防止旋轉圓柱管和二維圓柱模型中的應力集中和不連續擴散係數與濃度分布問題。二維圓柱模型管內表面的矽濃度可以轉化為氧化層，從而防止 LBE 等冷卻液在通過原管內部時進一步侵蝕 FGC 和 FGM 模型的內層結構。當 FGM 的體積分率值逐漸增加並且結構為 $Fe_{12}Cr_2Si$-SiC 之設計時，由最大剪應力理論計算的安全裕度也隨之提高。根據研究成果顯示，體積分率值為 3 的情況下 $Fe_{12}Cr_2Si$-SiC 的功能性材料模型是當今輕水型核反應爐管道設計的理想結構組合，該研究成果亦考慮到了 LBLOCA 意外發生時超過 1000℃高溫之問題。